Disentangling Enigmatic Gamma-Ray Sources

Bachelor's Thesis in Physics

Presented by

Tobias Müller

Date: 28.05.2024

Erlangen Centre for Astroparticle Physics
Friedrich-Alexander-Universität Erlangen-Nürnberg

Supervisor: Dr. Alison Mitchell

Abstract

Gamma ray sources are some of the most energetic objects in our Galaxy. Observing gamma rays entails challenges, yet a uniform description of one region is expected when observed with two different instruments at the same energy and within the uncertainties. An example of a discrepancy is shown by the analysis of the region around the pulsar wind nebula (PWN) HESS J1825-137 and HESS J1826-130 using data from the H.E.S.S. Galactic plane survey (HGPS), as well as data taken by the High-Altitude Water Cherenkov Observatory (HAWC). While the analysis of the HGPS data suggests only two sources in the region, the analysis of the HAWC data suggested a third source in between the two counterparts HAWC J1825-138 and HAWC J1826-128, HAWC J1825-134. In this thesis, the total energy flux in the region measured by both instruments is compared. The uncertainties from both studies are then used to minimize the difference in the observed energy flux. Through this method, we find that within uncertainties, the additional energy flux observed by HAWC and interpreted as a separate source, HAWC J1825-134, is consistent with the flux observed by HESS J1825-137. This work can therefore not support the claim of the detection of a third source between HESS J1825-137 and HESS J1826-130.

Contents

1 Introduction

Before 1912, it was believed that all the ionizing radiation in the atmosphere was originating from radioactive elements on earth. Victor Hess was the first person to connect the radiation with extraterrestrial sources. In the years 1911 and 1912, he performed several free balloon flights up to an altitude of over 5000 meters. During the ascent, he discovered decreasing ionization up to 1000 meters but an increasing ionization rate above. Hess ruled out the sun as a source after a balloon flight during a solar eclipse did not show a particular difference. This lead to the conclusion that there must be radiation coming from space. This radiation is what we now call cosmic rays (CRs). For this discovery, Hess received the Nobel Prize in Physics in 1936 [1]. Since then, the study of CRs has been a hot topic leading to lots of experiments explaining the features of the spectrum.
The rate of CRs bombarding Earth is about 1000 particles per square meter and second. The composition of CRs is energy dependent but generally, about 87% of those particles are protons, $\sim 12\%$ are alpha-particles and $\sim 1\%$ are nuclei of heavier elements. There is also a small abundance of leptonic components, being about 100 times less abundant. Figure 1 displays the all-particle energy flux of CRs observed on Earth. The spectrum is a power-law $\propto E^{-\alpha}$ with different spectral indices α within certain energy ranges. Up to about $\simeq 3 \times 10^{15}\,\text{eV}$, the so-called *knee*, the spectral index is $\alpha \approx -2.7$. After this, the spectrum softens to $E^{-3.1}$ up to the *second knee* at $\sim 2 \times 10^{17}\,\text{eV}$. The first knee marks the maximum energy up to which protons can be accelerated within our galaxy. The second knee represents the energy up to which iron, the heaviest cosmic-ray element, can be accelerated by the same mechanisms. At about $3 \times 10^{18}\,\text{eV}$, the spectrum flattens to $\alpha \approx -2.7$ again. This last break in the spectrum is called the *ankle*. Then, the spectrum cuts off at about $10^{20}\,\text{eV}$.
Particles with energies up to about $10^{17}\,\text{eV}$ are believed to originate from within our Galaxy. Ultra High Energy Cosmic Rays above $\sim 10^{18}\,\text{eV}$ arise from extragalactic sources [2] [3].

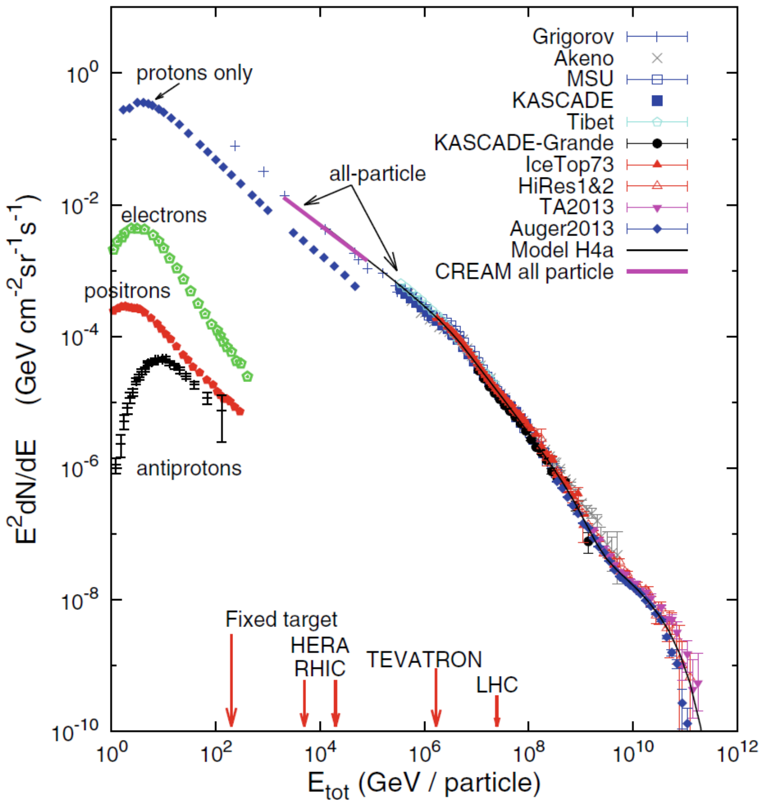

Figure 1: The all-particle CR energy flux. Taken from [3].

2 The origin of Gamma-Rays

To understand where gamma rays come from, one first must understand the origin of cosmic rays.

2.1 Origin of Cosmic Rays

The origin of cosmic rays is bound by some requirements for the object. These requirements include particle acceleration up to the knee at PeV energies, a fitting spectral index of the energy spectrum and a mean energy rate at Earth of $\sim 3 \times 10^{48}\,\mathrm{erg\,yr^{-1}}$ [4]. A candidate fitting these requirements are supernovae (SNe). A supernova happens at the end of the lifetime of a star when the pressure provided by burning atoms in the core is no longer sufficient to withstand the gravitational attraction of the star itself. The outer shell collapses onto the core of the star. In this process, cosmic rays are created. Other objects producing CRs include supermassive black holes, galaxy mergers or magnetized neutron stars.

2.2 Acceleration

While traveling through space, the CRs are getting accelerated through different mechanisms. One of these is the acceleration caused by collisionless shocks. This is called diffusive shock acceleration

(DSA) or first order Fermi acceleration. Other acceleration mechanisms are inductive acceleration in an ordered field or second order Fermi acceleration.

2.2.1 Supernova remnants

When the outer shell of the star collapses onto the core, a supernova remnant (SNR) is formed. The ejecta from the shell move supersonically through the surrounding medium with a shock wave leading in front. This is called the free expansion phase and is the first of four phases of a SNR. The Sedov-Taylor phase follows, in which the swept-up mass of the shell dominates over the ejected mass. The explosion energy is now stored as internal and kinetic energy of the expanding shell. After that, radiation losses take over in the pressure-driven phase. Lastly, there is the merging phase where the shock wave slowly disappears and the shell now moves subsonically [5]. With a typical energy of a supernova explosion of about 10^{51} erg and a rate of two to three SNe in our Galaxy per century on average, as well as the assumption that 10% of the kinetic energy released can be converted into particle acceleration, SNRs provide the experimentally derived energy rate of CRs [4].
In a supernova, the upstream region describes the region in front of the shock wave and is separated by the shock from the downstream region. The particle in the heated plasma of the downstream medium can cross the shock into the upstream medium due to magnetic-field irregularities acting as magnetic mirrors. In the upstream medium, the particle also diffuses until the shock overtakes it again and the process can repeat itself. During this process, the particle gains kinetic energy and can be accelerated to relativistic speeds. Therefore, SNRs are considered to be particle accelerators and may be capable of achieving PeV energies up to the knee [5].

2.2.2 Pulsar wind nebulae

When a star with a mass of $< 25 M_\odot$ collapses and undergoes a supernova explosion, a neutron star will be created in the core of the SNR. The rotating pulsar provides relativistic particles and magnetic fields and dominates the dynamics of the core area of the SNR. While the power of the rotating pulsar is related to that of an oscillating dipole, it is not expected to emit the same magnetic dipole radiation. This is due to the plasma of the pulsar, which prevents electromagnetic waves from propagating and instead propels a relativistic wind of electrons and positrons outward. A non-thermal, relativistic electron/positron plasma is formed and dominates the pressure in a spheroidal region around the neutron star. The pulsar wind nebula (PWN) results from electrons and positrons being accelerated at the shock front and expands freely into the interstellar medium.
Interactions of the SNR with the interstellar medium create a reverse shock wave which travels back to the center of the remnant on a timescale of about 10^4 years. The PWN expands and the outer edge runs into the reverse shock of the SNR, where, depending on the pressure difference between the PWN and the ejecta, the PWN may be crushed by the shocked ejecta and brightened, or the reverse shock may be prevented of moving inward.
A prominent example of a PWN is the Crab nebula with a rotation period of $P = 33.5\,\mathrm{ms}$ and an

age of $\sim 960\,\mathrm{yr}$. This age is known from historical records, while the characteristic age $\tau_{ch} = \frac{1}{2}\frac{P}{\dot{P}}$ is a calculated estimation and is about $1274\,\mathrm{yr}$ for the Crab [5].

2.3 Production of Gamma-Rays

Gamma rays can be produced by a variety of processes including leptonic and hadronic particles.
The first process is Bremsstrahlung. It occurs when charged particles are accelerated, decelerated or deflected in a Coulomb field. This leads to a change in the particle's trajectory while a photon is emitted. This process is favored for electrons over protons due to the interaction probability being proportional to $(m_p/m_e)^2$ and therefore being about 4×10^6 larger.
Synchrotron radiation is electromagnetic radiation that is emitted when a relativistic, charged particle is accelerated perpendicular to its velocity in a magnetic field B. Electrons are more affected by this process than protons because the characteristic energy is reduced by a factor of $(m_p/m_e)^3 \simeq 7 \times 10^9$ for protons. Additionally, stronger magnetic fields lead to a higher frequency of emitted photons.
Particles scattering off of photons can transfer energy to the photon. This process is called inverse Compton (IC) scattering. The uniform presence of the cosmic microwave background makes this process happen frequently. IC scattering of protons is suppressed by a factor of $(m_e/m_p)^4$ compared to that of electrons. The transfer of energy from an electron to a $2.7\,\mathrm{K}$ CMB photon can produce gamma rays up to tens of TeV. The process is more likely to happen at high energies since the cross-section only depends on the product $k = \epsilon_e \cdot \omega$ of the interacting electron energy ϵ_e times the target photon energy ω:

$$\sigma_{\mathrm{IC}} \simeq \frac{8}{3}\sigma_{\mathrm{T}}\frac{\ln(4k)}{k} \qquad k \gg 1, \tag{1}$$

with the Thomson cross-section $\sigma_{\mathrm{T}} \simeq 6.65 \times 10^{-25}\,\mathrm{cm}^2$.
Lastly, protons interacting with other protons in the interstellar medium produce pions. While all pions π^+, π^0 and π^- are produced in this process, only π^0 decays into gamma rays: $\pi^0 \longrightarrow \gamma\gamma$. The energy of the π^0 created is about 20% of the proton initial energy, giving the γ-rays an energy of $E_\gamma \simeq 0.1 E_p$ each [3].
Gamma rays produces by these processes propagate through space and can end up at Earth. The following chapter explains methods used to detect gamma rays that enter Earth's atmosphere.

3 Gamma-ray detection methods

γ-rays that enter earth's atmosphere cannot be detected as such from the ground. They interact with particles in the atmosphere, creating an air shower. These can be used by ground-based observatories to observe γ-rays. As opposed to γ-ray telescopes in space, ground-based telescopes can be built much larger and thus observe higher energies, because there is no constrain on getting the material on site. There are two types of methods used to detect γ-rays from the ground: Imaging Atmospheric Cherenkov Telescopes (IACTs) and water-Cherenkov detectors (WCDs). In the following chapter, the process of air showers and instruments used to detect γ-rays are described in detail.

3.1 Air showers

Cosmic rays and gamma rays undergo interactions in the atmosphere. These interactions in the atmosphere are different when triggered by charged energetic nuclei from CRs or high-energy γ-rays. The interaction of CR protons with the atmosphere results in the production of charged and neutral pions among other particles. These pions then further decay into muons and neutrinos in case of a charged pion and in case of a neutral pion into two photons, which can then result in pair production of electron-position pairs. This results in an air shower with hadronic and electromagnetic components, which spreads widely and irregularly due to the large amount of transverse momentum transfer during the hadronic interactions.

Gamma rays on the other hand produce electron-positron pairs in the upper atmosphere at an altitude of about 20 km. These electrons and positrons can produce gamma rays again as a result of Bremsstrahlung, which then again produce electron-positron pairs and so on. This goes on until the electrons of the final generation have too little energy to continue the process, cool down and become thermalized. This so-called electromagnetic Air Shower exists for about 10^{-4} s and is confined in its extent to an approximately axial symmetry.

The opening angle of the air shower cone is about 1° and increases the farther the particles descend. At the ground, the radius of this "light pool" is about 125 m. The maximum number of shower particles is reached at an altitude of about 10 km before it dies out later [6]. Figure 2 shows a comparison of the two shower types simulated with Monte Carlo simulations by Völk and Bernlöhr, 2008 [7]. The difference in broadness and irregularity of the showers is apparent [7].

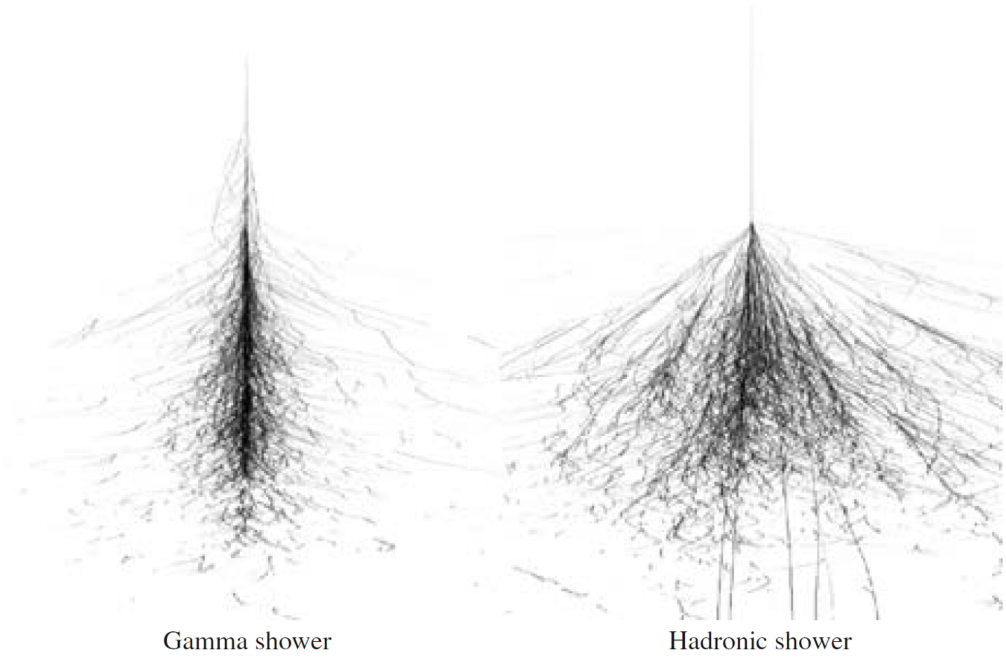
Gamma shower

Hadronic shower

Figure 2: Comparison between a gamma shower and a hadronic shower. Taken from Völk and Bernlöhr, 2008 [7]

3.2 Cherenkov light

When a charged particle travels through a medium, it is possible for it to have a higher speed than the speed of light in that medium and thus emit Cherenkov light. The speed of light in a medium depends on the index of refraction of the medium n_m and equals $c_m = \frac{c}{n_m}$. For air at standard pressure and temperature, the speed of light is $c_{air} = c/1.0003 = 0.9997c$. A charged particle moving in a certain direction emits Cherenkov light, mostly in the ultraviolet spectrum, in a small cone around the direction of motion.

In an air shower, relativistic charged particles obey this behavior and each emit about 10 to 20 Cherenkov photons per meter. Considering there are about 10^8 to 10^9 charged particles in an air shower, large amounts of ultraviolet Cherenkov photons are produced in the direction of the air shower [8]. Since the particles carry a speed above the speed of light in the medium, the Cherenkov light trails behind the particles. In air, this effect is small because the index of refraction is close to 1, so the time difference between photons and the particles is only about 2 ns [7].

3.3 Imaging Atmospheric Cherenkov telescopes

Imaging Atmospheric Cherenkov telescopes (IACTs) measure the Cherenkov radiation from air showers using mirrors to collect the photons and channel them onto a camera. Hereby, the hadronic air showers produced by CRs make up the background that needs to be separated from the gamma showers in order to have a clear signal of the gamma ray source. It is to mention that the flux of CR particles is, in general, about a factor of 1000 higher than that of gamma rays, making the signal isolation a large difficulty. The different properties of the two shower types can be used to differentiate the signal from the background. In Figure 3, the same scenario as in Figure 2 is displayed from the sensor's point of view. A gamma shower creates a small, symmetric signal, while a proton shower creates a much larger and non-uniform signal. These characteristics are used to identify gamma ray signals.

The image of a 100 m^2 telescope only provides about 100 photoelectrons for a γ-ray event with an energy of 100 GeV, assuming a conversion efficiency of 10% [7]. Note that the number of Cherenkov photons is about proportional to the energy of the initial γ-ray. The low energy threshold of the detector is therefore determined by its photon detection efficiency.

A large field of view of the detector is needed due to the large area covered by the light pool [6]. Also, in order to be able to differentiate between hadronic and γ-ray showers, a sufficient amount of photomultiplier tubes (PMTs) should be present in the camera, so the difference between the two can be properly detected [9].

A single telescope is limited in its abilities. To overcome these limitations, multiple telescopes are used as one observatory. This method is called the stereoscopic technique. All telescopes coincidentally observe one event and project each image onto one plane. Doing so allows the direction of the primary γ-ray to be determined by taking the intersection of the major axis of each image. This way,

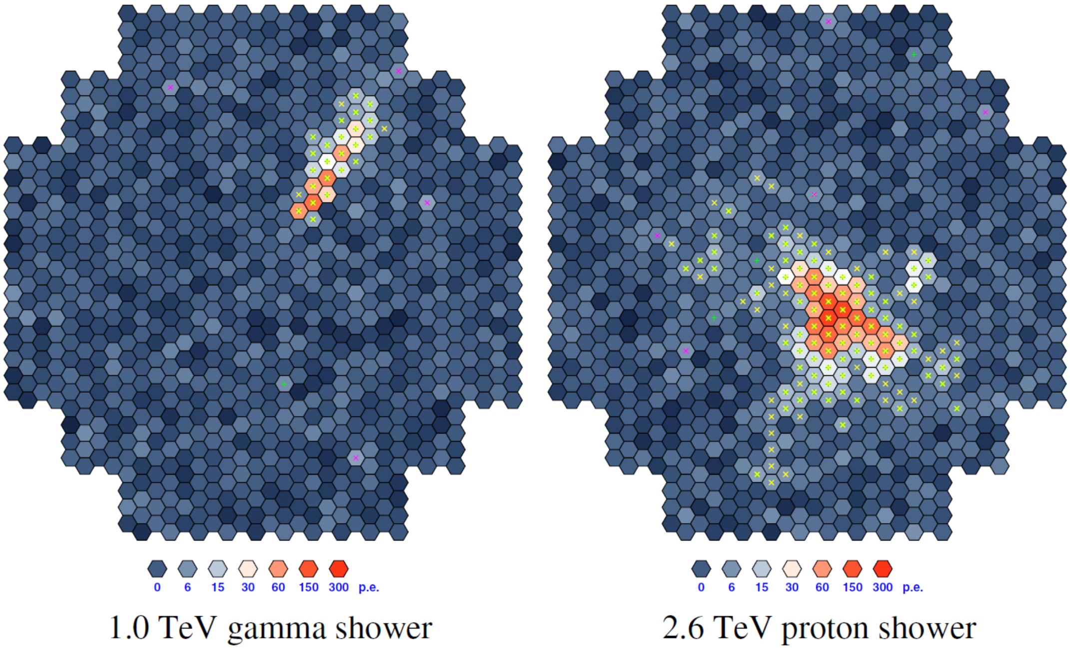

Figure 3: Images of air showers created by an incoming photon (*left*) and by an incoming proton (*right*) in the camera. Taken from Völk and Bernlöhr, 2008 [7].

hadronic showers can be excluded when, e.g., a muon is observed by one of the telescopes. Figure 4 shows the images of an air shower from four individual telescopes and the combined image with the reconstruction of the primary γ-ray direction. Additionally, using the stereoscopic technique improves the angular and energy resolution, the background rejection and the sensitivity and allows for a three-dimensional model of the air shower to be created [7].

IACTs are pointing instruments, i.e., they have a narrow field of view and need to be pointed at the objected that is being observed. Additionally, since they are optical instruments, they can only operate during nighttime and good weather conditions and thus have a low duty cycle of about 5 to 10% [8].

H.E.S.S. The High Energy Spectroscopic System (H.E.S.S.) is located in the Khomas highland of Namibia at an altitude of 1800 m above sea level. In the first phase, four IACTs were placed in a square formation with a side length of 120 meters (H.E.S.S. Phase I). These telescopes have a combined area of 107 m^2 and a camera, each with 960 photomultipliers per telescope. At zenith, the energy threshold is roughly 200 GeV, increasing with an increasing zenith angle. A fifth, much larger telescope was added at the center of the array in the second phase (H.E.S.S. Phase II) in 2012 [10]. The 600 m^2 dish of the fifth telescope increases the energy coverage, sensitivity and angular resolution of H.E.S.S. Additionally, a camera with 2048 photomultipliers is used for observations [6]. The data in this thesis was solely collected in the first phase, i.e. the fifth telescope was not used.

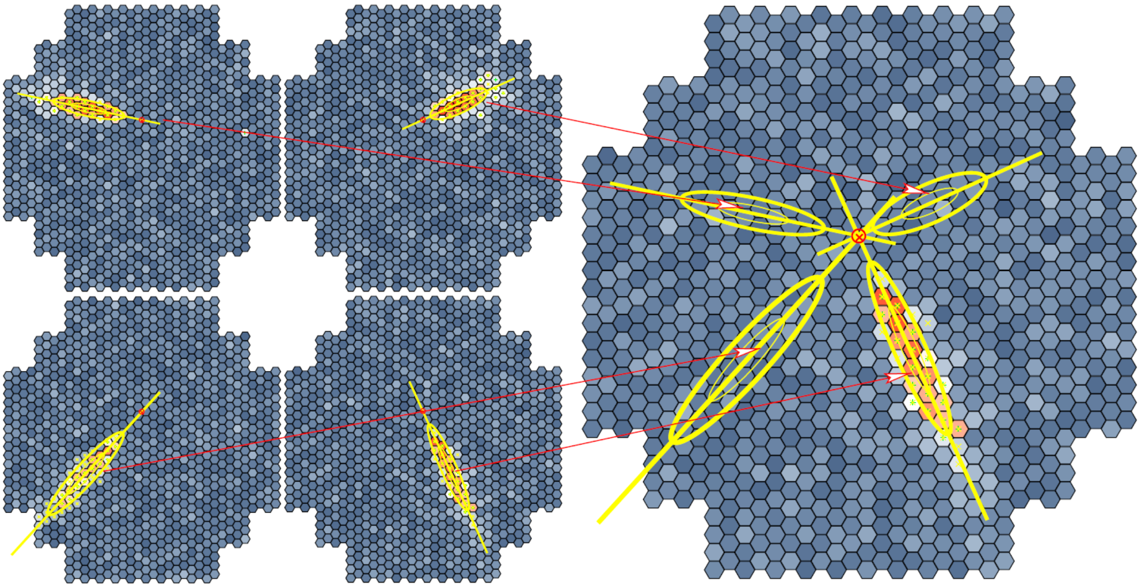

Figure 4: Reconstruction of the direction of the initial γ-photon from an IACT with detectors arranged in an array of four telescopes. Taken from Völk and Bernlöhr, 2008 [7].

3.4 Water Cherenkov Detectors

Water Cherenkov detectors (WCDs) are not optical instruments like IACTs, but they observe the shower particles that actually reach the ground. For that, water tanks are built at high altitudes to collect more particles before the shower dies down. WCDs use the higher index of refraction of water and the resulting speed of light in water of $0.77c$. When relativistic particles hit the water molecules, they pass kinetic energy to the water molecules, which are accelerated to higher speeds than the speed of light in water and thus emit Cherenkov light. This way, CR showers and gamma ray showers can be detected. The CR particles overwhelm the γ-ray signal by a factor of 1000, as discussed before. To avoid the unwanted background, a large area of WCDs is set up. The measured detections in each detector and the known position relative to all other WCDs allow a differentiation between the less extended gamma showers and the widely spread hadronic showers. This makes it possible to separate CRs from gamma-rays. Additionally, taking the timing between the detections into account, it is possible to find the direction of the primary particle.
WCDs are survey instruments with a large field of view and no constraints depending the weather or time of the day. Thus, the duty cycle is usually above 90% [8] [11].

HAWC The High Altitude Water Cherenkov (HAWC) observatory is an instrument in Sierra Negra, Mexico, sensitive to multi-TeV hadron and γ-ray air showers. Located at an altitude of 4100 m are 300 instrumented water tanks covering an area of $22,000\,\mathrm{m}^2$ (see Figure 5, *right*), each made up of a 7.3 m diameter and 5 m tall tank filled with purified water up to a depth of 4.5 m, leaving 4 m of water above each PMT. The detectors are three 8-inch PMTs in an equilateral triangle of side length 3.2 m, with a fourth 10-inch PMT at the center of the triangle at the bottom of the tank (see Figure 5, *left*). HAWC is able to detect γ-rays in an energy range from hundreds of GeV to hundreds of TeV in about two-thirds of the gamma-ray sky, thanks to its location and large field of view. The angular resolution ranges from 0.1° to 1.0° [11] [12].

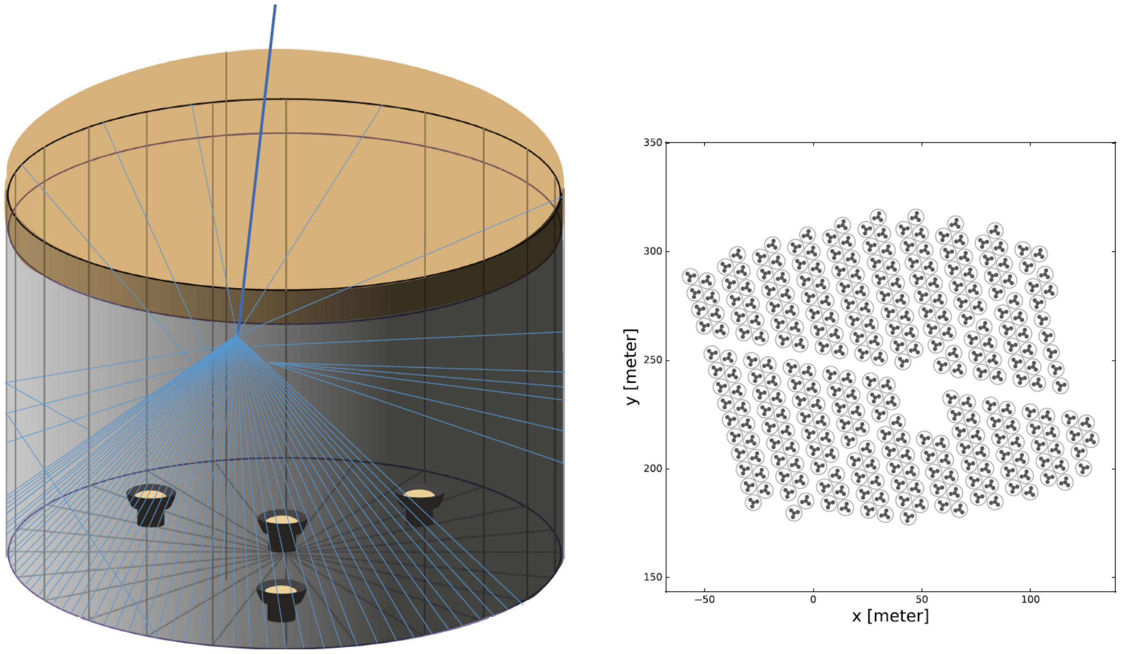

Figure 5: Schematics of the HAWC instrument. On the *left*, one single water tank is shown. The *right* shows the complete layout of the HAWC. The large circles are the WCDs and the small circles the individual PMTs. This figure is taken from Abeysekara et al., 2017 [12].

IACTs vs. WCDs Both methods of observing γ-rays have different advantages and disadvantages. Below 1 TeV, only a few particles reach the ground while Cherenkov photons are still well detectable. Therefore, the energy threshold of IACTs is lower than that of WCDs. Also, WCDs can operate in all weather conditions and at all times but it's much harder to distinguish between CR air showers and γ-ray air showers. On the other hand, IACTs have a small field of view and can only operate during nighttime and good weather, since they are optical instruments [8]. The sensitivities of the two instruments H.E.S.S. and HAWC are displayed in Figure 6. These curves are taken from Hinton and Ruiz-Velasco (2020, [13]) and Funk et al. (2013, [14]) and represent the 100 hour and 1 to 5 year sensitivity curves for a point source for H.E.S.S. and HAWC, respectively. The behavior in sensitivity at different energies between IACTs and WCDs are apparent: H.E.S.S. is more sensitive at lower energies while HAWC becomes more sensitive at high energies. In this thesis, no sources are point-like, therefore drawing firm conclusions about the observability cannot be made with certainty.

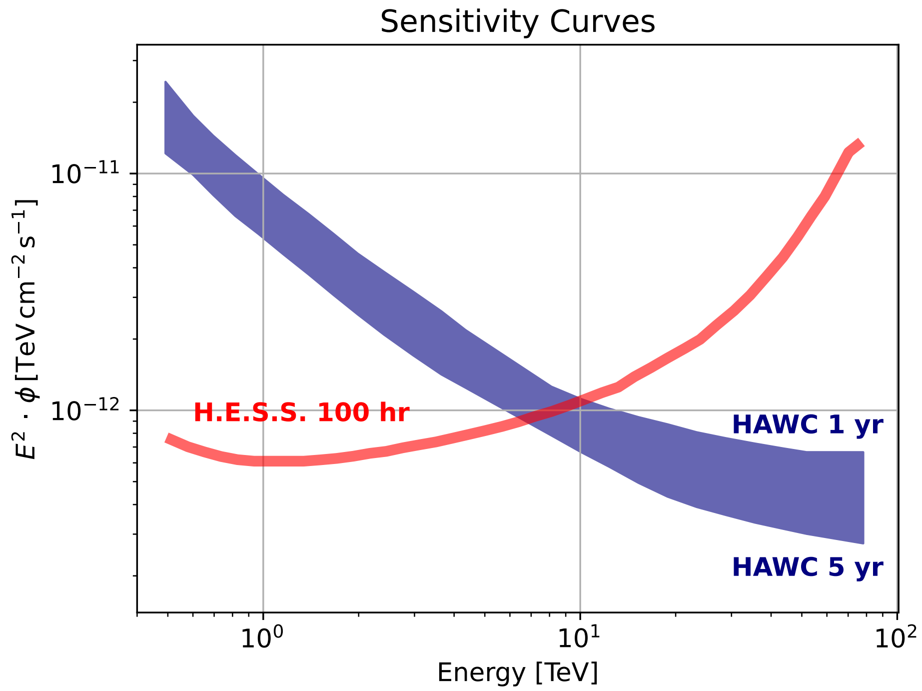

Figure 6: Differential flux sensitivity of H.E.S.S. and HAWC to point-like sources, observed for 100 hrs and one to five years respectively. The curves were taken from Hinton and Ruiz-Velasco 2020 [13] and Funk et al. 2013 [14].

4 HESS J1825-137 / HESS J1826-130

The region consists of 3 sources: HESS J1825-137, HESS J1826-130 and LS 5039. Both H.E.S.S. sources are associated with PWNe. LS 5039 is a point-like gamma-ray binary, also detected in X-ray and radio, and lies south of the other two sources and will not be considered for this study [15].

HESS J1825-137 HESS J1825-137 is a PWN with an unusual large size and a strong energy-dependent morphology at VHE γ-rays. The extent measured in [16] is given by the radial distance from the pulsar at which the flux reaches $1/e$ of the maximum flux in an energy band. According to this, the extent of HESS J1825-137 varies from $0.37°\pm0.18°$ at $< 125\,\mathrm{GeV}$ to a maximum extent of $0.76°\pm0.23°$ at $250 - 500\,\mathrm{GeV}$ and decreases to $0.14°\pm0.15°$ above $32\,\mathrm{TeV}$. The total γ-ray flux of the source is $\sim 64\%$ of the flux of the Crab nebula, equivalent to $\sim 1.12 \pm 0.28\,\mathrm{cm^{-2}\,s^{-1}}$ [16]. It is located at a distance of roughly $3.9\,\mathrm{kpc}$ and is associated with the young pulsar PSR J1826-1334 [17] with a spin-down age of $\tau = 2.14 \times 10^4\,\mathrm{yr}$, a spin-down power of $\dot{E} = 2.8 \times 10^{36}\,\mathrm{erg\,s^{-1}}$, a period of $P = 0.1015\,\mathrm{s}$ and a characteristic age of $21\,\mathrm{kyr}$ situated at a distance of $\sim 4\,\mathrm{kpc}$ [16]. The latest observations in X-ray with *Suzaku* identify a compact core with an extended component with diffuse X-ray emission up to $17\,\mathrm{pc}$ or $15'$ from the pulsar [18]. Prior X-ray observations with *XMM-Newton* (X-ray Multi-Mirror Mission) found the compact core to extend $30''$ and a diffuse component extending $5'$ as well as an asymmetric morphology [19]. In infrared ($8\,\mu\mathrm{m}$ and $24\,\mu\mathrm{m}$) and radio ($1.4\,\mathrm{GHz}$) there are no visible counterparts of the nebula observed [16] [20].

HESS J1826-130 HESS J1826-130 used to be considered a part of HESS J1825-137 [21] due to its close proximity which contaminates the spectral measurements by up to $\sim 41\%$. It is associated with the X-ray "Eel" PWN and the slightly offset (by 0.09°) pulsar PSR J1826-1256 that is one of the brightest radio-quiet γ-ray pulsars known. Located at a distance of 1.55 kpc, it has a spin-down power of $\dot{E} = 3.6 \times 10^{36}\,\mathrm{erg\,s^{-1}}$, a period of $P = 0.110\,\mathrm{s}$ [16] and a characteristic age of 14.4 kyr [22]. HESS J1826-130 has an extension of 0.15°±0.02° which also includes SNR G18.6-0.2 [23] with a diameter of 0.1°. It is unclear if G18.6-0.2 is associated with HESS J1826-130. Wether the gamma ray emission is of leptonic or hadronic origin has not been fully identified yet [10].

4.1 Data

The data used for this thesis is from two papers: The H.E.S.S. Galactic plane survey (HGPS) [10] and Albert et al. 2021 [24]. They follow a similar modeling for the sources using a Gaussian spatial model and power-law and exponential cutoff power-law spectral models. The Gaussian spatial model is defined as such:

$$S_{\mathrm{Gauss}}(r|\phi, \sigma) = \phi \frac{1}{2\pi\sigma^2} \exp\left(-\frac{r^2}{2\sigma^2}\right), \tag{2}$$

with the surface brightness S_{Gauss}, the total spatially integrated flux ϕ, the width σ of the Gaussian component and the offset $r = \sqrt{(\ell - \ell_0)^2 + (b - b_0)^2}$ (with respect to the position (ℓ_0, b_0)).
The power-law (PL) spectrum is given by

$$\phi(E) = \phi_0 \cdot \left(\frac{E}{E_0}\right)^{-\Gamma}, \tag{3}$$

with the differential photon flux $\phi_{\mathrm{ref}}(E)$ at a reference (pivot) energy E_0 and the spectral index Γ. The exponential cutoff power-law (ECPL) is defined using the inverse cutoff energy $\lambda = 1/E_{\mathrm{cutoff}}$:

$$\phi(E) = \phi_0 \cdot \left(\frac{E}{E_0}\right)^{-\Gamma} \cdot \exp(-\lambda E). \tag{4}$$

4.1.1 The H.E.S.S. Galactic plane survey

The HGPS [10] is a survey of the Galactic plane done from 2004 to 2013 in the very high-energy γ-rays. Its total observation time is 2864 hours with a total livetime of 2673 hours with an average dead time of 6.7%. A range from longitudes $\ell = 250°$ to $65°$ and latitudes $|b| =\leq 3°$ are included. Figure 7 shows the region of the survey overlaid as a white rectangle over an all-sky image of *Planck* CO(1-0) data from the Planck Collaboration X, 2016 [25]. The map below shows the γ-ray flux of all sources above 1 TeV and with a sensitivity above 10% Crab flux and the observation time in hours. The sources found in this region are listed in a VHE γ-ray source catalog (Table A.7 and Table A.8 in [10]), which is publicly available and used for the analysis of the H.E.S.S. sources, with their corresponding morphology and spectrum. Galactic sky maps are also publicly available and are used to visualize the differential flux of the region above 1 TeV in this thesis.

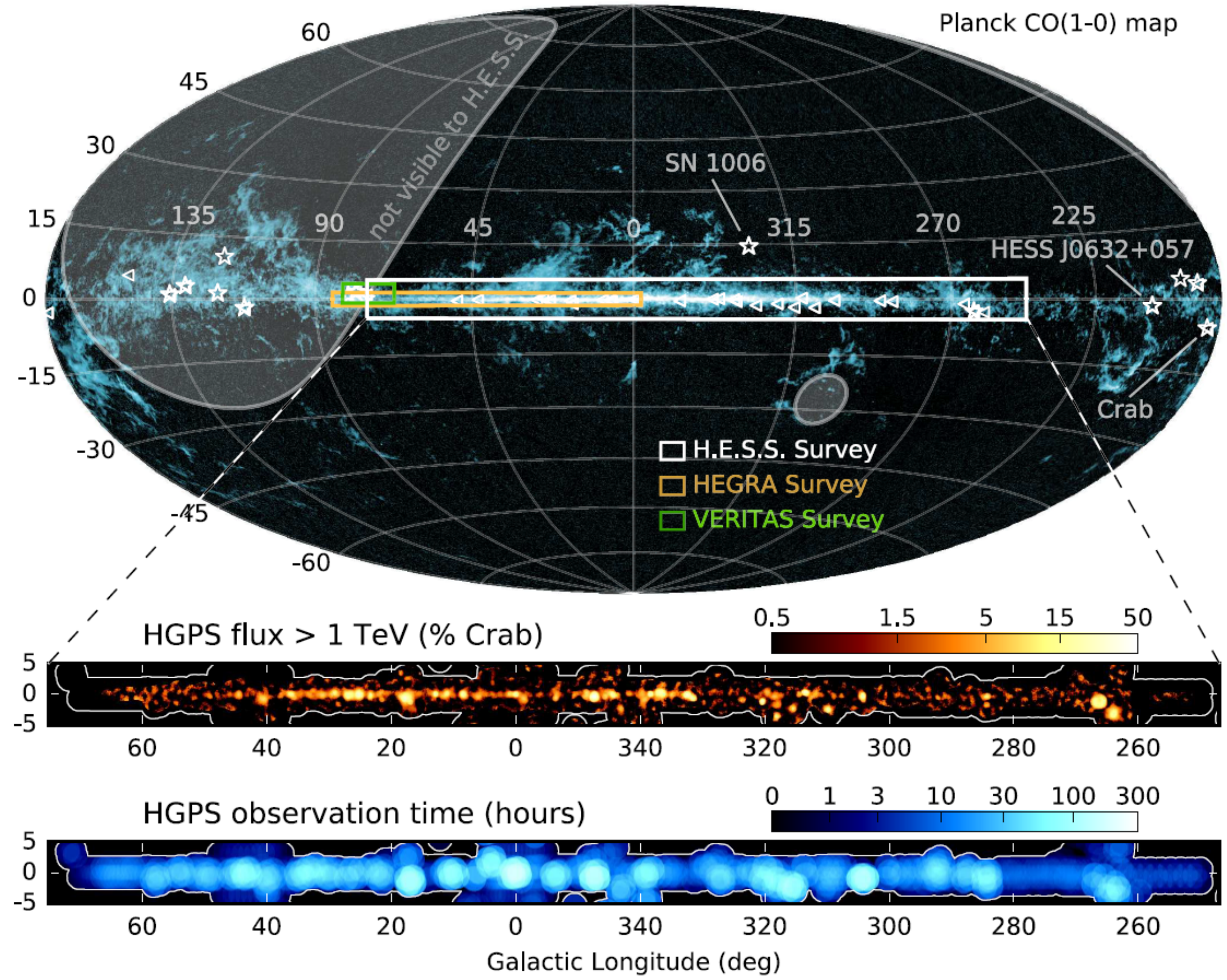

Figure 7: All-sky image of *Plank* CO(1-0) data (Planck Collaboration X 2016 [25]). The HGPS region is indicated by the white rectangle. Depicted below is the γ-ray flux of all sources above 1 TeV for regions observed with a sensitivity above 10 % Crab flux and the observation time in hours. The white outline shows the boundary of the survey region [10].

The HGPS source catalog contains 78 sources of which 14 are not analyzed in the H.E.S.S. survey. All other sources are fitted with one or more, depending on their morphology, two-dimensional symmetric Gaussian model which deduces the position, size and flux. The data for the two sources HESS J1825-137 and HESS J1826-130 is shown in Table 1 where for the spectral model, only parameters and their respective errors are shown that are regarded in this thesis. The other parameters include the reference energy E_0 and the inverse cutoff energy λ whose values are stated later. HESS J1825-137 is divided up into three gaussian components due to its energy dependent morphology. The spectral model is only given for the whole source in the source catalog. Therefore, assuming the spectral model is the same for all components, the total integrated flux value ϕ needs to be calculated for each component. This is done by taking the share of each differential flux given in [10] of the HESS J1825-137 differential flux as a whole. HESS J1826-130 is described by a power-law function as in Equation 3 and the components of HESS J1825-137 by an exponential cutoff power-law as in Equation 4. The inverse cutoff energy λ is $0.07^{+0.02}_{-0.02}\,\mathrm{TeV}^{-1}$ and the reference energy is 0.65 TeV for

Source Name	GLON [°]	GLAT [°]	Width [°]	ϕ [cm^{-2} TeV^{-1} s^{-1}]	Γ
HESS J1825-137					
Comp. 1	$16.99^{+0.09}_{-0.09}$	$-0.49^{+0.04}_{-0.04}$	$0.48^{+0.03}_{-0.03}$	$1.9^{+0.6}_{-0.6} \times 10^{-11}$	$2.15^{+0.26}_{-0.26}$
Comp. 2	$17.712^{+0.025}_{-0.025}$	$-0.660^{+0.014}_{-0.014}$	$0.391^{+0.017}_{-0.017}$	$4.5^{+0.5}_{-0.5} \times 10^{-11}$	$2.15^{+0.26}_{-0.26}$
Comp. 3	$17.841^{+0.009}_{-0.009}$	$-0.706^{+0.009}_{-0.009}$	$0.109^{+0.009}_{-0.009}$	$5.9^{+1.0}_{-1.0} \times 10^{-12}$	$2.15^{+0.26}_{-0.26}$
HESS J1826-130	$18.48^{+0.10}_{-0.10}$	$-0.39^{+0.10}_{-0.10}$	$0.152^{+0.021}_{-0.021}$	$2.7^{+0.5}_{-0.5} \times 10^{-13}$	$2.0^{+0.3}_{-0.3}$

Table 1: Data of HESS J1825-137 and HESS J1826-130 from the HGPS source catalog. HESS J1825-137 consists of 3 gaussian components while HESS J1826-130 consists of a single gaussian.

every component of HESS J1825-137 and 2.06 TeV for HESS J1826-130.

Figure 8 displays the spectral models, the sum of the spectral models and the HAWC sensitivity introduced earlier for comparison. Both HESS J1826-130 and the third component of HESS J1825-137 are mostly below the 5-year HAWC sensitivity and should therefore not be entirely observable with HAWC. Since the sensitivity curves depicted here are calculated for point-like sources, these conclusions should be taken with a grain of salt and may not represent an actual physical truth.

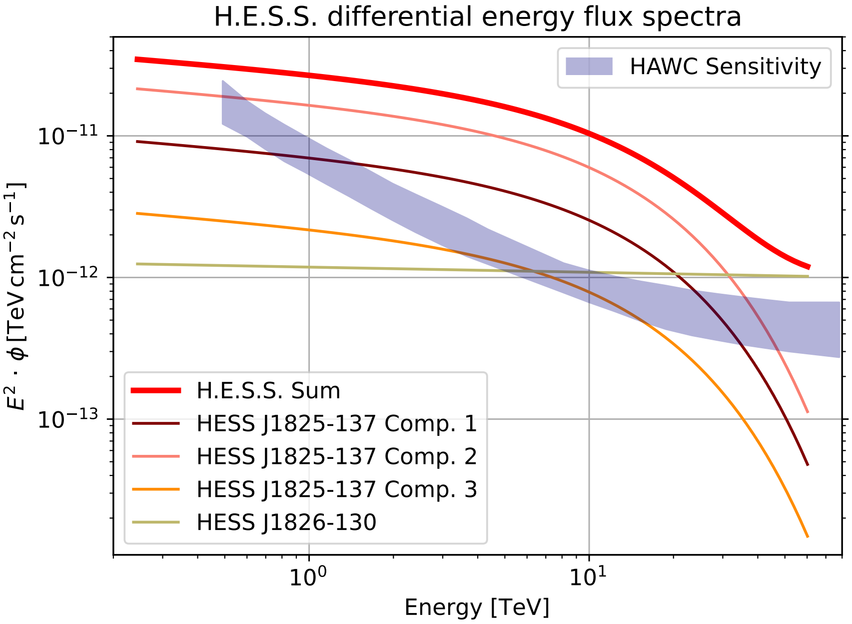

Figure 8: The spectral models used to describe the emission from HESS J1825-137 and HESS J1826-130, as derived in the HGPS [10]. Overlaid is the 5 year HAWC point-source sensitivity.

4.1.2 HAWC analysis of the region

The analysis done with the HAWC observatory used is by Albert et al. 2021 [24]. The dataset contains 1343 observation days with a general uptime of the detector of $> 90\%$. A third HAWC source is claimed to have been found in the region: HAWC J1825-134. The energy spectrum appears to extend beyond 200 TeV with no cutoff hence a power-law spectral model (Equation 3) is utilized.

Exponential cutoff power-law spectral models describe the other two sources HAWC J1825-138 and HAWC J1826-128. Additionally, a Galactic diffuse emission (GDE) component that is gaussian-shaped along the Galactic latitude $b = 0°$ with a size of 1° from previous HAWC studies (Rho et al. 2017 [26]), is included in the analysis. The spatial models are gaussian models for HAWC J1825-138 and HAWC J1826-128 and a point-source model for HAWC J1825-134. An upper limit of 0.18° on the size of HAWC J1825-134 is given with a 95% confidence level. Since a smaller spatial bin size, corresponding to the resolution of HAWC, is used for the analysis applied in this work, a gaussian model with a size of 0.18° will be used to describe this emission in from here on. Table 2 lists the parameters of the three HAWC sources. The errors on the Galactic longitude and latitude are not given because the systematic error of 0.2° on the absolute pointing for the region is considered instead. Also, the size of HAWC J1825-134 does not include an error due to it being an upper limit. The cutoff energies are 27^{+21}_{-11} TeV for HAWC J1825-138 and 24^{+25}_{-14} TeV for HAWC J1826-128 with a pivot energy of 18 TeV.

Source Name	GLON [°]	GLAT [°]	Width [°]	$\phi\,[\mathrm{cm^{-2}\,TeV^{-1}\,s^{-1}}]$	Γ
HAWC J1825-138	17.67	-0.67	$0.47^{+0.06}_{-0.09}$	$4.5^{+2.5}_{-3.0} \times 10^{-14}$	$2.02^{+0.34}_{-0.42}$
HAWC J1826-128	18.61	-0.31	$0.20^{+0.03}_{-0.05}$	$2.7^{+2.4}_{-2.2} \times 10^{-14}$	$1.2^{+0.8}_{-0.9}$
HAWC J1825-134	18.09	-0.52	0.18	$4.2^{+1.9}_{-2.2} \times 10^{-15}$	$2.28^{+0.22}_{-0.16}$

Table 2: Data of HAWC J1825-138, HAWC J1826-128 and HAWC J1825-134 from Albert et al. 2021 [24]. The errors on the Galactic longitude and latitude are not used in this thesis are therefore not displayed. Only an upper limit on the size of HAWC J1825-134 is available which is used as the size of a gaussian spatial model.

Figure 9 shows the spectral models of the three HAWC sources as well as the combined spectral model. Also, the 100 hours H.E.S.S. sensitivity for point sources is added. All HAWC sources are above the sensitivity in the considered energy range from 1 to 10 TeV and should be detectable by H.E.S.S.

4.1.3 Best-fit models

Figure 10 displays all the original best-fit models from HGPS and the HAWC survey on the differential flux map of the region as derived in the HGPS [10]. The H.E.S.S. components are depicted in black with the spatial model of HESS J1825-137 being separated into three Gaussian components. Sources observed by HAWC are pink, with their sizes as dashed pink lines. The newly discovered source HAWC J1825-134 sits between the two H.E.S.S. sources and slightly overlaps with HAWC J1825-138.

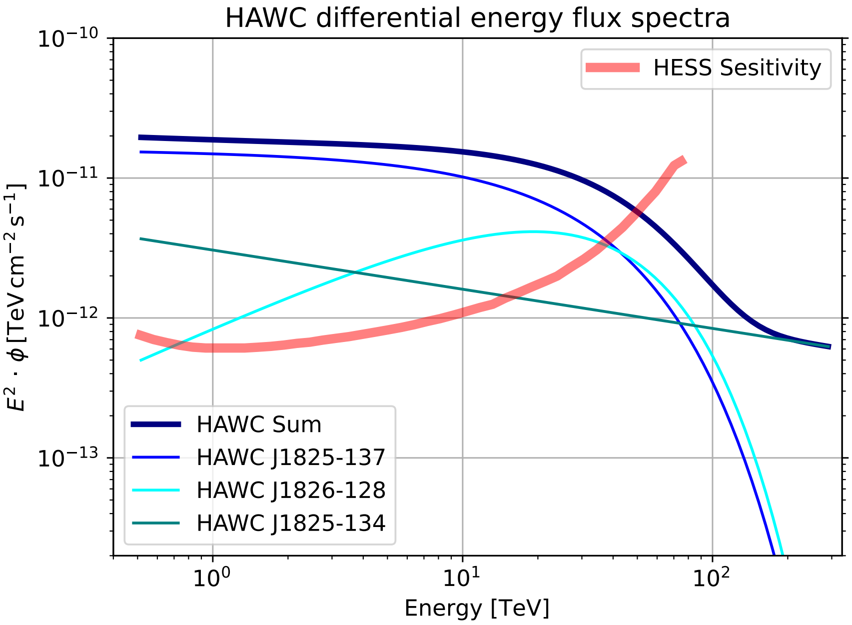

Figure 9: Spectral models of the three HAWC sources HAWC J1825-138, HAWC J1826-128 and HAWC J1825-134 from Albert et al. 2021 [24]. The 100 hour point-source sensitivity for H.E.S.S. is overlaid.

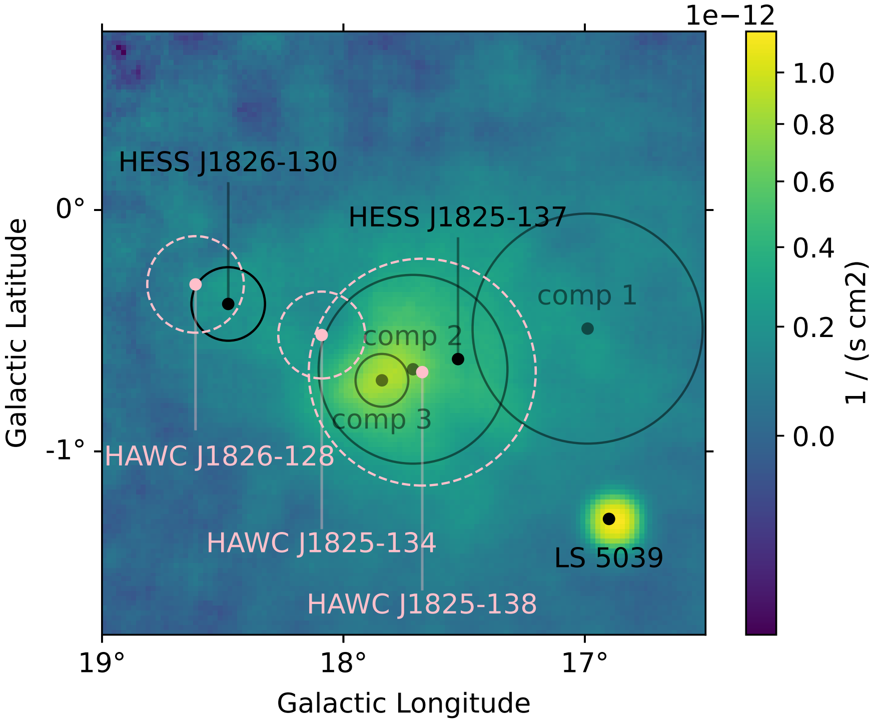

Figure 10: Differential flux map of the region, as derived in [10]. The best-fit positions of the gamma-ray sources observed by HAWC and H.E.S.S. are indicated by the pink dashed and black circles, respectively.

5 Systematic uncertainties and total energy flux

Uncertainties on the measurements are the basis of this thesis. Apart from the statistical uncertainties, the systematic uncertainties play an important role in the analysis of the data. Below, the origin of the systematic uncertainties of both instruments will be discussed.
The HAWC analysis considered systematic errors from HAWC studies by Abeysekara et al. 2017 [12] and 2019 [27]. Several effects on the systematic uncertainty are considered.

1. The angular resolution discrepancy, which is thought to be caused by the reconstruction of the shower curvature model that is not energy dependent. This effect is approximately 5% at maximum and negligible at high energies.

2. Late light simulation is the dominant source of uncertainty and is due to a mismodeling of the late light, i.e. a difference between the time structure of the air shower and the time width of the calibration laser pulse.

3. The charge uncertainty provides the error on the variation of measurements with PMTs for a fixed amount of light and the differences between the detection efficiency across PMTs. It is not a major source of uncertainty.

4. The absolute PMT efficiency is one of the dominant sources of systematic uncertainty. It is determined by matching the peak position of vertical muons to an expected position concluded from Monte Carlo simulations since it cannot be precisely established with the calibration system.

5. PMT threshold is the lowest charge a PMT can detect. Its effect on the uncertainty differs for different thresholds.

6. Lastly, additional 10% of uncertainty are added to account for other systematic uncertainties.

None of these effects have a correlation and hence can be added in quadrature to the others. For more detail see Abeysekara et al. 2017 [12] and 2019 [27].
H.E.S.S. includes a systematic uncertainty of the PSF of 0.03° taken from a bias on point-like extragalactic sources. The spectral parameters of observations underlie various systematic uncertainties like the atmospheric transparency, the calibration and the event reconstruction as well as the analysis method itself. A relative systematic uncertainty on the flux from the maps and from the spectra of 30% and an absolute systematic uncertainty of 0.2 on the spectral index is assumed.
Apart from these systematic uncertainties, statistical uncertainties are accounted for in all errors stated. Systematic and statistical uncertainties are added in quadrature to result in the total error.

In order to estimate the comparability of the results derived from measurements of the region by HAWC and HESS, the energy flux difference between both measurements is minimized within the respective uncertainties of the detectors. As discussed earlier, the sources show an energy dependent morphology. Taking this energy dependence into account is a great endeavor that exceeds the realms of this thesis. Therefore, an energy range of 1 TeV up to 10 TeV, corresponding to a range covered by both H.E.S.S. and HAWC was chosen. This energy range will be used in this thesis.

First the process of minimizing the energy flux will be discussed. The energy flux is calculated using Gammapy. The class "SkyModel" is used to create a spatial and spectral model as described in subsection 4.1 for each source. The associated method "evaluate_geom" evaluates the energy flux at every pixel within a given map geometry. The geometry is given by the position of the region and a chosen width that includes all sources. The position is chosen as a galactic longitude of $\ell = 17.75°$ and a galactic latitude of $b = -0.5°$ and the width is 2.5° which covers all sources by H.E.S.S. and HAWC. From this, all fluxes are calculated.

The HAWC observations consider an additional third source, so the total energy flux of the region, observed by HAWC, ϕ_{HAWC} is considered to be higher than the total energy flux observed by H.E.S.S. ϕ_{HESS}. Thus, the difference in energy flux in the region is calculated by subtracting the sum of the energy flux of the H.E.S.S. components from the sum of the energy flux of the HAWC sources:

$$\Delta\phi = |\phi_{\mathrm{HAWC}} - \phi_{\mathrm{HESS}}| \tag{5}$$

with the total spatially integrated flux $\phi_{\mathrm{HESS}} = \sum_0^3 \phi_{\mathrm{HESS,i}}$ and $\phi_{\mathrm{HAWC}} = \sum_0^4 \phi_{\mathrm{HAWC,i}}$ for the components in Table 1 and Table 2. This is done for every single pixel in the geometry separately and summed up over all pixels to give the energy flux difference between H.E.S.S. and HAWC for the entire region.

Then, the systematic uncertainties on the source position, extension and spectral properties derived in the respective analysis [10], [24] are taken into account to minimize delta F. The following sections will discuss each of these processes in greater detail.

5.1 Grid positions

The grid of points around the respective positions of each component is constructed from the systematic uncertainty on the best-fit position for each source as given in Table 1. For each source, the given error on the galactic longitude $\Delta\ell$ and latitude Δb is taken as the axes of an ellipse:

$$\frac{\ell^2}{\Delta\ell^2} + \frac{b^2}{\Delta b^2} = 1.$$

The spacing between each grid point for the H.E.S.S. sources is 0.02°, given by the angular resolution of H.E.S.S. This results in $2 \cdot \Delta\ell/0.02° + 1$ points in the longitudinal axis and $2 \cdot \Delta b/0.02° + 1$ points in the latitudinal axis. The factor 2 describes the entire number of points on one axis, in opposed to only the minor or major axis given by $\Delta\ell$ or Δd. Since the positions are considered to be on the grid points, one has to be added to take the original best-fit position into account.

Albert et al. (2021, [11]) found that there is a systematic error from the HAWC observations on the absolute pointing for the region exceeding the uncertainties on the best-fit positions. Therefore, the error on the absolute pointing of 0.2° is considered as the error on the galactic longitude $\Delta\ell$ and latitude Δb while other errors are neglected. The spacing of 0.1° for the grid points of the HAWC

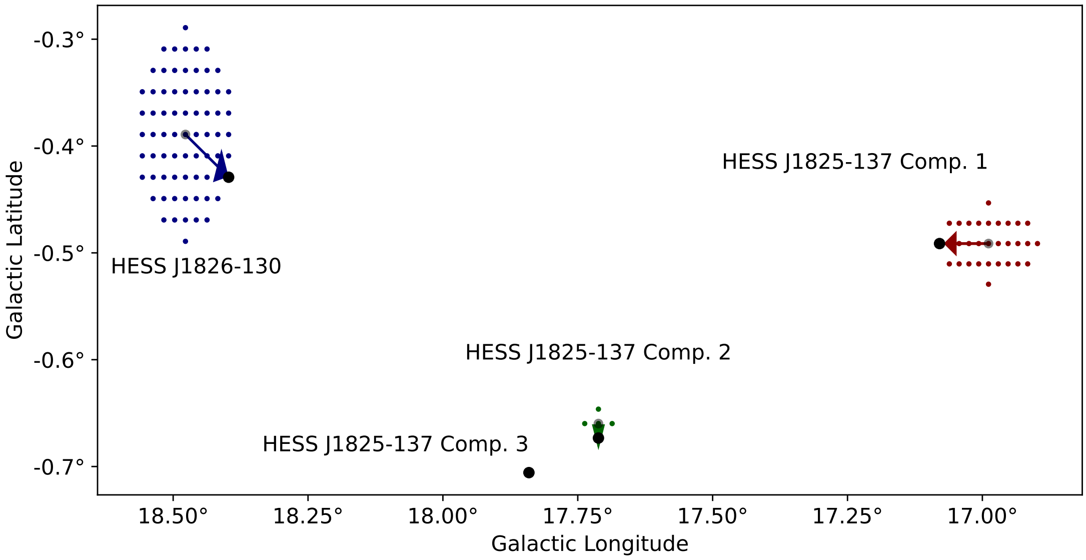

Figure 11: The grid of positions that are tested for the H.E.S.S components. The dimension of the grid for each component is given by the systematic uncertainties on the best-fit position. The distance between two grid points is 0.02°, given by the angular resolution of H.E.S.S. resulting in all shown grid points. The arrows indicate the positions minimizing the flux in the region.

sources is given by the best angular resolution achieved by HAWC (Abeysekara et al. 2019 [27]). The grid of points for the H.E.S.S. and HAWC components are shown in Figure 11 and Figure 12 respectively. For each new position of one source, the flux is minimized relative to every new position of every other source as described above. The arrows indicate the positions for which the energy flux difference in the region is minimal.

5.2 Size

The size of a gaussian spatial model is described by its containment radius σ as given in Equation 2. The uncertainties on the size are given in Table 1 and in Table 2 as the width for all H.E.S.S. and HAWC components, respectively. The angular resolution of each observatory again defines the dimension of sizes tested, where in this case the number of sizes for each source is rounded to the nearest natural number to avoid having a very low amount of widths tested. In Figure 13 and Figure 14 all H.E.S.S. and HAWC sources are shown with their associated possible sizes. The black dashed lines represent the best-fit width derived in the respective analysis, the green lines describe the largest and the red lines the smallest widths within the rounded uncertainties. The number of sizes is determined by the error on the size for each source individually and is rounded to the closest natural number. The difference of the sizes is 0.02° for H.E.S.S. and 0.1° for HAWC, which corresponds to the angular resolution of H.E.S.S. and the best angular resolution of HAWC found by Abeysekara et al. 2019 [27]. It is notable that only one of the three HAWC sources, i.e. HAWC J1825-138, has

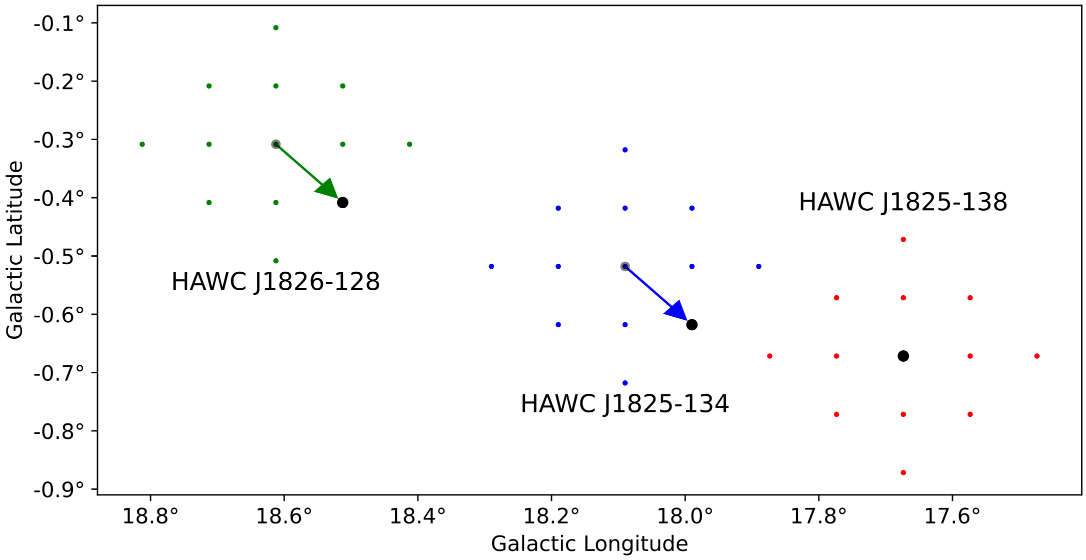

Figure 12: The grid of points within a circle of 0.2° radius for the HAWC sources. The radius corresponds to the systematic error on the absolute pointing for the region and was determined in studies for the third HAWC catalog by Abeysekara et al. 2019 [27]. The spacing of the grid points of 0.1° is taken as the lowest angular resolution of HAWC from the 3HWC catalog. The arrows indicate the positions minimizing the flux in the region.

an error within the angular resolution to allow for different sizes, while H.E.S.S. allows three of the four components to have a different width. That is due to the lower angular resolution of H.E.S.S. Then, $\Delta\phi$ is again calculated for each of these combinations of different sizes, to identify the minimal energy flux differences for different source extensions. The size of each component minimizing the energy flux best will result.

5.3 Spectral model

The components can be described by either a power-law (Equation 3) or an exponential cutoff power-law model (Equation 4). In this thesis, the uncertainties on the amplitude ϕ_0 and on the spectral index Γ are considered. This is sufficient since the cutoff energy lies outside of the energy range for all components and thus all exponential cutoff power-law models behave like a power-law model inside the energy range. The spacing of the errors is correlated to the energy resolution of the telescope. For H.E.S.S., this is 14% [28] and for HAWC an estimated energy resolution of 70% is assumed. This estimation is done due to the strong energy dependence of the energy resolution in the energy range of 1 TeV to 10 TeV [8]. The amount of models for each error then results from the energy resolution depending on the value of the parameter. On the example of component 1 of HESS J1825-137, the amplitude is $1.89 \times 10^{-11}\,\mathrm{cm}^{-2}\,\mathrm{TeV}^{-1}\,\mathrm{s}^{-1}$ which results in a spacing of $2.65 \times 10^{-12}\,\mathrm{cm}^{-2}\,\mathrm{TeV}^{-1}\,\mathrm{s}^{-1}$. With an error on the amplitude of $\pm 0.554 \times 10^{-12}\,\mathrm{cm}^{-2}\,\mathrm{TeV}^{-1}\,\mathrm{s}^{-1}$ the number of amplitudes is 2 for the positive and negative sign and additionally the original amplitude, equaling 5 amplitudes tested.

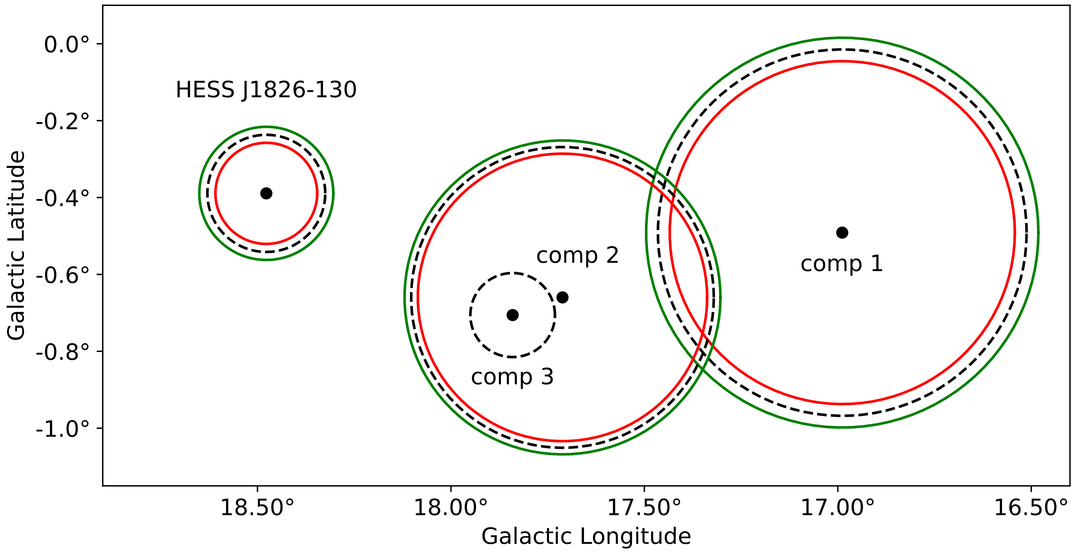

Figure 13: The sizes of the H.E.S.S. components. The green line is the largest size while the red one is the smallest. The black dashed line describes the best-fit size.

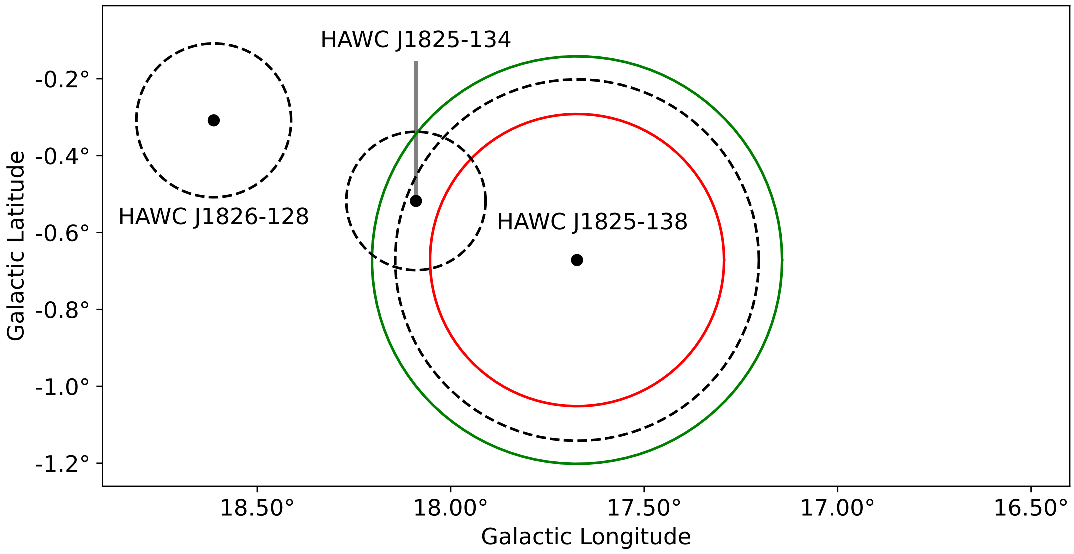

Figure 14: The sizes of the HAWC components. The green line is the largest size while the red one is the smallest. The black dashed line describes the best-fit size.

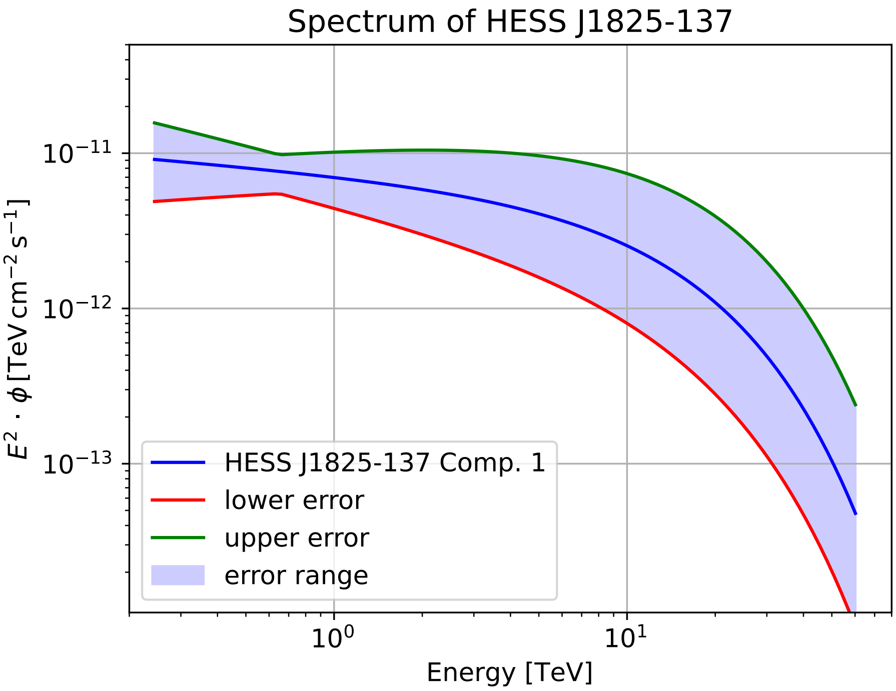

Figure 15: Spectrum of Component 1 of HESS J1825-137 in [10], the systematic errors on the spectrum are indicated by the shaded band. The green line describes the maximum positive error in amplitude and index up to the kink where the positive error in amplitude and negative error in index take over. The red line describes the same scenario with the opposing signs of errors.

The same process is done for the spectral index and all other sources.
Figure 15 shows the best-fit spectral model, as well as the systematic error on the spectral model, of component 1 of HESS J1825-137. The green line describes the highest energy flux for component 1 within the systematic uncertainties. A spectral model at this line will not follow the line along the kink, which is solely a result of regarding both errors simultaneously, but it will follow the curve up to the kink and continue steadily. The same yields for the lowermost red curve.

6 Results

To get the best models minimizing the sum of the energy flux difference, every method described above must be applied after one another. Hereby, the order of the methods used first, second and last play a role in the minimization process.

Order of flux minimization In order to have a clear result, the three methods of minimizing the energy flux difference have to be tested in every possible order. Table 3 shows the results of the minimization process for the energy flux for every possible order, as well as the original sum of the energy flux difference between the HAWC and H.E.S.S. observations of the region. Minimizing

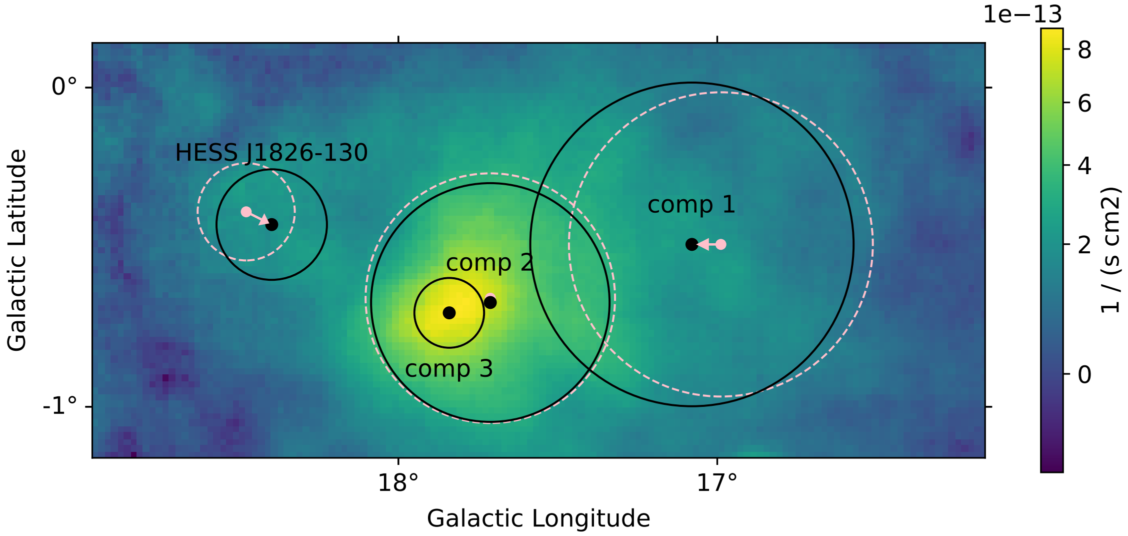

Figure 16: Differential flux map as derived in the HGPS. The new H.E.S.S. positions, minimizing the flux difference between the measurements conducted by H.E.S.S. and HAWC, are shown as black circles. Original positions and sizes are shown as pink dashed circles.

the energy flux using the spectral model first gives the worst results, while adjusting the size first results in the lowest difference. This may be due to size changing the energy flux most. Finding the best fitting sizes for all sources first gives the possibility to adjust the other parameters accordingly. Overall, the lowest difference in energy flux is achieved by the order of adjusting the sizes first, the positions second and lastly the spectral models. Using this order a value of 185.36 $\mathrm{TeV^{-1}\,cm^{-2}\,s^{-1}}$ can be achieved compared to a value of 570.18 $\mathrm{TeV^{-1}\,cm^{-2}\,s^{-1}}$ for the original best-fit models. That is equivalent to a reduction of 67.5% from the original energy flux difference.

Energy flux differences [$\mathrm{TeV^{-1}\,cm^{-2}\,s^{-1}}$]

Original	P S SM	P SM S	S P SM	S SM P	SM P S	SM S P
570.18	239.35	256.21	223.10	185.36	372.47	380.57

Table 3: The sum of the energy flux differences for every order of the three methods compared to the original energy flux difference according to Equation 5. (P) stands for the position or method of grid points, (S) for size and (SM) for spectral model.

In Figure 16 and Figure 17 the results can be seen for the H.E.S.S. and HAWC components, respectively. The original models from HGPS and from Albert et al. 2021 [24] are pictured in pink, with the sizes being represented by dashed pink circles around the sources. The pink arrows indicate the change of the position if transpired and the black lines and dots describe the best results found by this thesis. All the HAWC components shift into the same direction which is to be expected since the systematic error on the absolute pointing was considered as the error on the positions instead of individual errors on the position.

Comparing the original best-fit spectral models (Figure 8 and Figure 9) to the best results within the errors in Figure 18 reveals a change in most spectral models. It is important to note that the

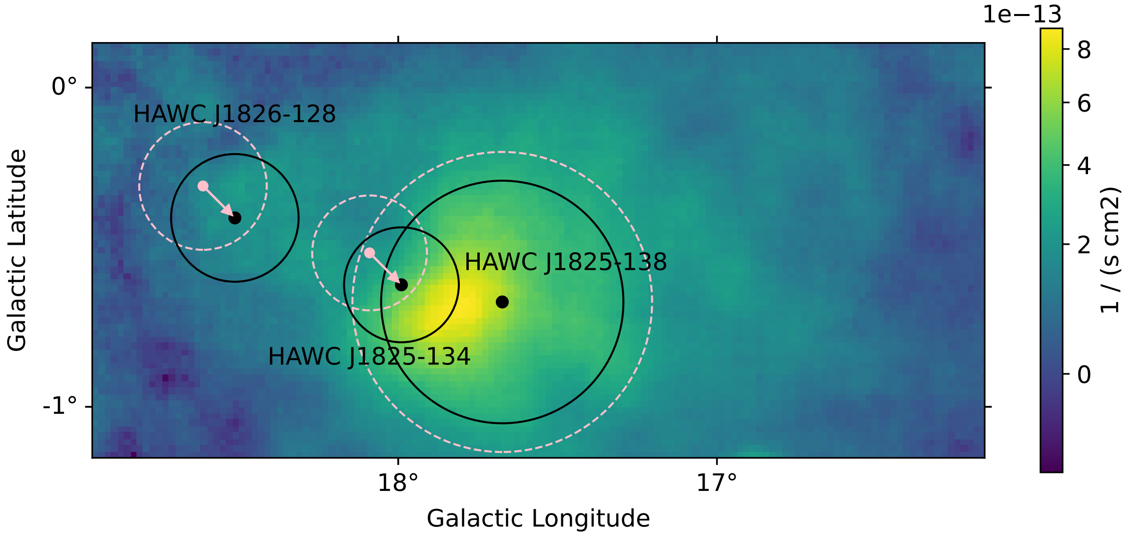

Figure 17: Differential flux map as derived in the HGPS. The new HAWC positions, minimizing the flux difference between the measurements conducted by H.E.S.S. and HAWC, are shown as black circles. Original positions and sizes are shown as pink dashed circles.

only energy range where the models from this thesis are valid is from 1 TeV to 10 TeV. The behavior below and above this range are not studied here. All mentioning of the spectral models will only refer to this energy range.

The sum of the spectral models flatten and are almost identical between H.E.S.S. and HAWC. HESS J1825-137 component 3 and HESS J1826-130 move entirely below the HAWC sensitivity curve, whereas before they were located above the 5-year sensitivity for the higher half of the energy range. Component 2 also shift to lower flux values while component 1 shifts to higher fluxes, which leads to the sum of the resulting best-fit H.E.S.S. spectral models consisting mostly of component 1.

The spectral models of the HAWC sources change less severely. HAWC J1825-137 gains in energy flux, while HAWC J1826-128 loses flux. This changes the percentage share of the sources to be weighted more on one source, just as for the H.E.S.S. sources. HAWC J1826-128 moves almost entirely below the 100 hour H.E.S.S. sensitivity curve.

All the resulting fit values for each source and component are listed in Table 4.

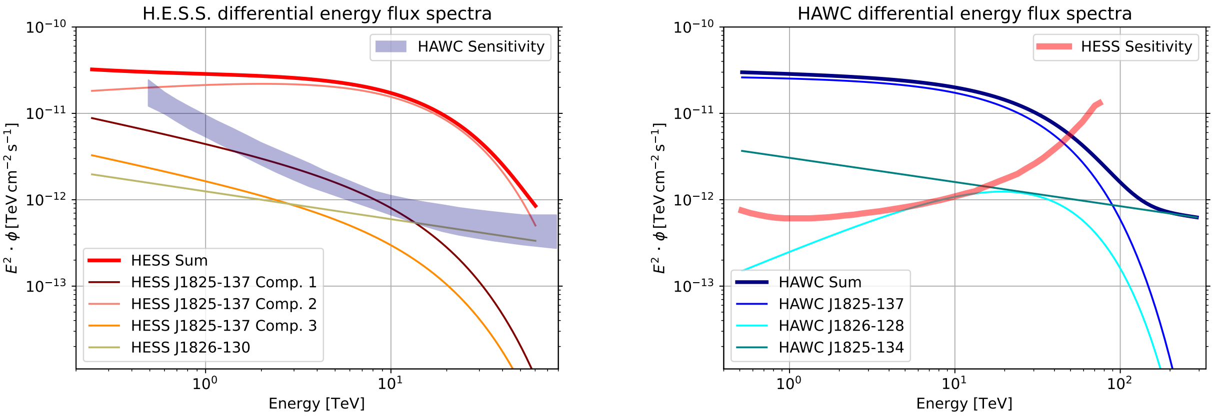

Figure 18: Spectral models after minimizing the flux difference between HAWC and H.E.S.S. observations for the H.E.S.S. components (*left*) and the HAWC sources (*right*). For reference, the original spectral models are shown in Figure 8 (H.E.S.S.) and Figure 9 (HAWC).

Source Name	GLON [°]	GLAT [°]	Width [°]	ϕ [cm^{-2} TeV^{-1} s^{-1}]	Γ
HESS J1825-137					
Comp. 1	17.08	−0.49	0.51	1.4×10^{-11}	2.45
Comp. 2	17.712	−0.673	0.374	5.1×10^{-11}	1.85
Comp. 3	17.841	−0.706	0.109	5.06×10^{-12}	2.45
HESS J1826-130	18.40	−0.43	0.173	2.3×10^{-13}	2.3
HAWC J1825-138	17.67	−0.67	0.38	7.7×10^{-14}	2.02
HAWC J1826-128	18.51	−0.41	0.20	8.1×10^{-15}	1.2
HAWC J1825-134	17.99	−0.62	0.18	4.2×10^{-15}	2.28

Table 4: Fit values of HESS J1825-137, HESS J1826-130 and HAWC J1825-138, HAWC J1826-128 and HAWC J1825-134 after minimizing the flux difference. The previous best-fit values are listed in Table 1 and Table 2 for the H.E.S.S. and HAWC sources, respectively.

6.1 Comparison with the original data

The models can be displayed in Gammapy using maps. With the map geometry introduced earlier, a 125 × 125 pixel map is created and the energy flux data of the models displayed. Such maps are shown in Figure 19. The original best-fit models are shown in the upper two panels, while the lower two panels show the new best-fit models obtained in this thesis, all normalized with the maximum flux value observed in the respective analysis. HAWC's observation of the region appears dimmer, while H.E.S.S. observes a bright central spot in HESS J1825-137.
The results from looking at the uncertainties and adjusting the positions, sizes and spectral models to minimize the sum of the energy flux difference, show a better accordance to one another. The bright peak in HESS J1825-137 is now also visible with HAWC J1825-134 in the HAWC region. The outer sources HESS J1826-130 or HAWC J1826-128 shift inward and merge with the other sources.

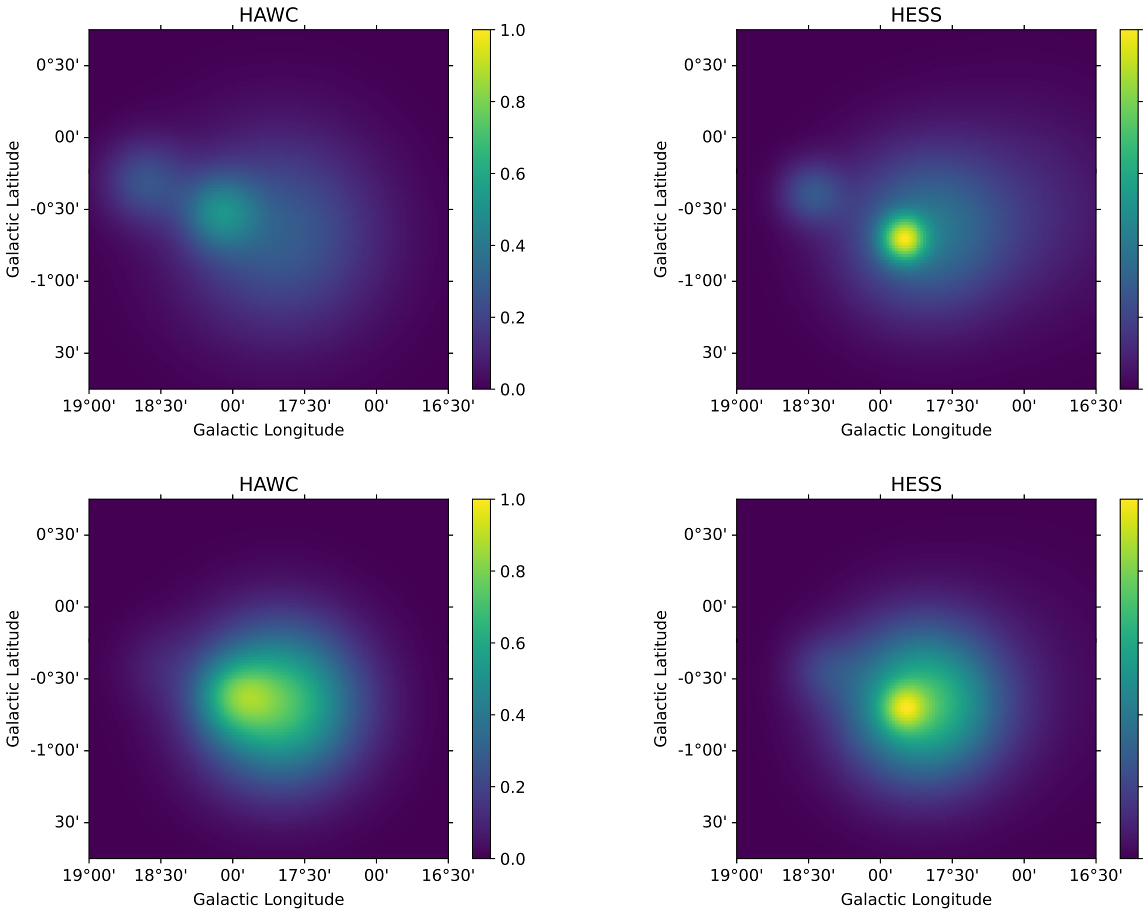

Figure 19: Relative energy flux of the region. The HAWC models are found on the *left*, H.E.S.S. models on the *right*. The original models are at the *top* and the best models minimizing the flux difference at the *bottom*.

This may not represent the physical properties of this object, but is merely a result from ignoring all other characteristics and only taking the energy flux into account.

To compare the sizes and positions of the sources, Figure 20 shows the best-fit positions of the source components of the original best-fit positions on the *top* and the new positions of the components after minimizing the flux difference on the *bottom* on the flux map estimated in the HGPS. Component 1 of HESS J1825-137 appears to be almost completely neglected by the HAWC sources, while the size of HAWC J1825-138 after minimizing the flux difference, is comparable to the size of component 2 of HESS J1825-137. Additionally, a more comparable description of the flux from HESS J1826-130 and HAWC J1826-128 is achieved.

Finally, Figure 21 shows the percentages of each component relative to the respective total integrated flux of the region as observed by the respective instrument after minimizing the flux difference. As seen before, the two HAWC sources HAWC J1825-138 and HAWC J1825-134 make up about as much flux in the region and energy range as the source HESS J1825-137, with 97.8% and 96.6%,

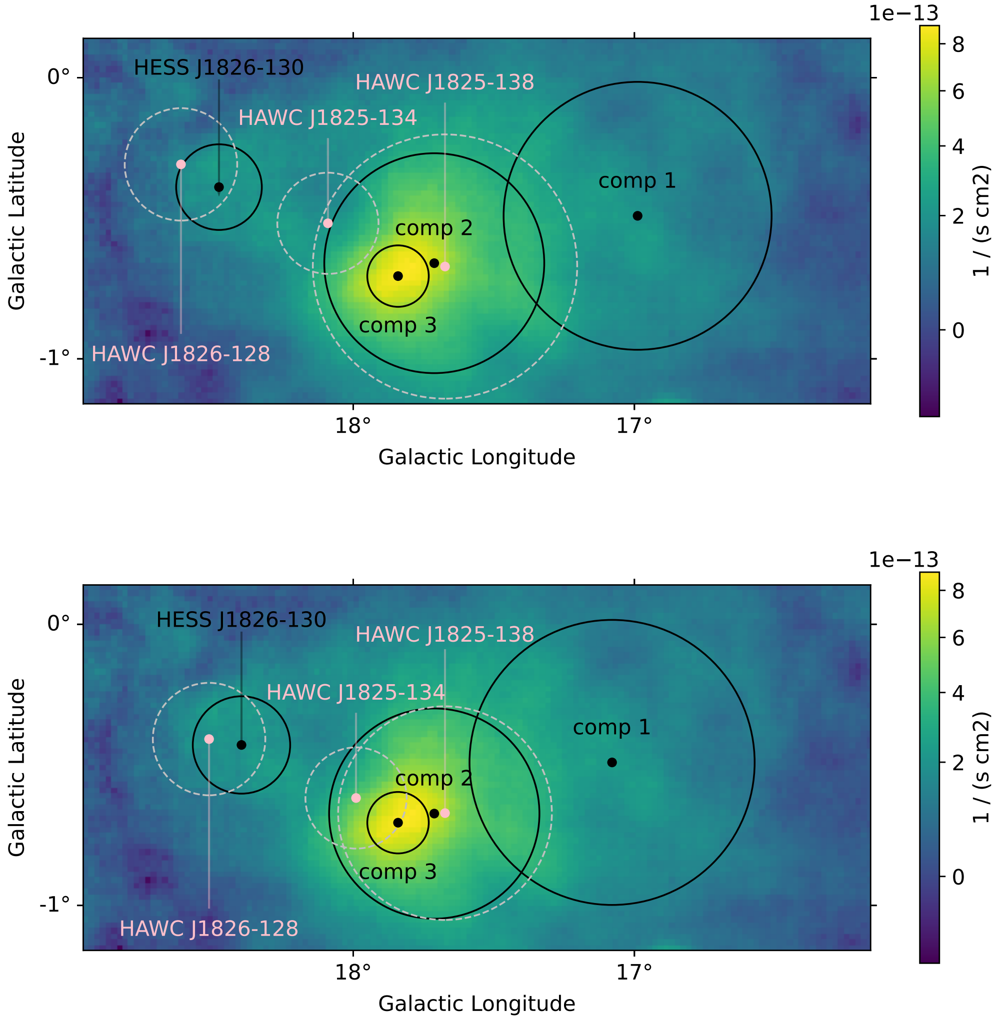

Figure 20: Flux map estimated in the HGPS, with the best-fit positions of the source components overlaid. *Top*: The original best-fit positions of the components derived in [24] in pink and dashed and the best-fit positions derived in [10] in black. *Bottom*: The new positions of the components after minimizing the flux difference.

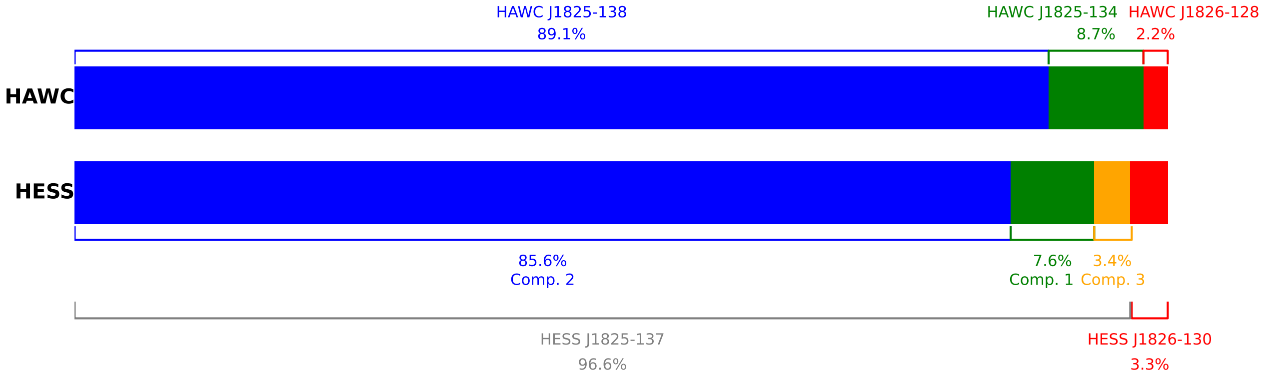

Figure 21: A comparison between the flux of the different components after minimizing the flux difference, relative to the overall flux observed by the respective instrument.

respectively. The other sources, HAWC J1826-128 and HESS J1826-130 remain with 2.2% and 3.3%, respectively.

7 Conclusion

This thesis presents an analysis of the discrepancy of H.E.S.S. and HAWC observations in the region around the H.E.S.S. sources HESS J1825-137 and HESS J1826-130. HAWC observations of the same region propose another source HAWC J1825-134 in the region apart from the counterparts HAWC J1826-128 and HAWC J1825-138 to the aforementioned H.E.S.S. sources. This new source leads to disagreements of the physical nature of the region.
In this work, the uncertainties on the reported parameters of all detected sources in the region were taken into account and a model to minimize the energy flux difference between the observations made by H.E.S.S. and HAWC in the region within said uncertainties was used. In order to do so, the influence of the position and extension of the sources, as well as their spectral models on the energy flux difference was examined. This work finds that, within the uncertainties of the fit parameters reported in the respective analysis, no significant energy flux difference can be found, and a spatial distribution of source components can be achieved that does not allow to undoubtedly distinguish the third HAWC source HAWC 1825-134 from the H.E.S.S. components of HESS J1825-137. Therefore, the third HAWC component HAWC J1825-134 may be fully explained by HESS J1825-137 and its components.

To achieve a clearer view of the sources and physical properties of the region, more observations need to be done. While HAWC J1825-134 may be part of the same PWN as HESS J1825-137, it is not beneficial to draw conclusions from simply adjusting the parameters. Since this region contains one of the brightest radio-quiet γ-ray pulsars, it will be an interesting target for future observations.

References

[1] P. H. Pleijel. *The Nobel Prize in Physics 1936 Award ceremony speech.* https://www.nobelprize.org/prizes/physics/1936/ceremony-speech/. Accessed: 2024-05-26. Dec. 1936.

[2] T. K. Gaisser, R. Engel, and E. Resconi. *Cosmic Rays and Particle Physics.* Vol. 2nd Revised edition. Cambridge University Press, 2016. isbn: 978-0-521-01646-9.

[3] S. Celli. *Gamma-ray and Neutrino Signatures of Galactic Cosmic-ray Accelerators.* Springer Cham, 2021. isbn: 978-3-030-33126-9.

[4] Z. A. Elmar. "A detailed study of the unidentified TeV source HESS J1826-130 in the search for Galactic PeVatrons with H.E.S.S." PhD thesis. Friedrich-Alexander-Universität Erlangen-Nürnberg, 2018.

[5] J. Vink. *Physics and Evolution of Supernova Remnants.* Springer Cham, 2020. isbn: 978-3-030-55231-2.

[6] *HESS: High Energy Stereoscopic System.* https://www.mpi-hd.mpg.de/HESS/. Accessed: 2024-05-26.

[7] H. J. Völk and K. Bernlöhr. "Imaging very high energy gamma-ray telescopes". In: *Experimental Astronomy* 25.1, 3 (Mar. 2009), pp. 173–191. issn: 1572-9508. url: http://dx.doi.org/10.1007/s10686-009-9151-z.

[8] *HAWC: the High-Altitude Water Cherenkov Observatory.* https://www.hawc-observatory.org/. Accessed: 2024-05-26.

[9] A. M. Hillas. "Cerenkov Light Images of EAS Produced by Primary Gamma Rays and by Nuclei". In: *19th International Cosmic Ray Conference (ICRC19), Volume 3.* Vol. 3. International Cosmic Ray Conference. Aug. 1985, p. 445.

[10] H.E.S.S. Collaboration et al. "The H.E.S.S. Galactic plane survey". In: *A&A* 612 (2018), A1. url: https://doi.org/10.1051/0004-6361/201732098.

[11] A. Albert et al. "3HWC: The Third HAWC Catalog of Very-high-energy Gamma-Ray Sources". In: *The Astrophysical Journal* 905.1, 76 (Dec. 2020), p. 76.

[12] A. U. Abeysekara et al. "Observation of the Crab Nebula with the HAWC Gamma-Ray Observatory". In: *Astrophysical Journal* 843.1, 39 (July 2017), p. 39.

[13] J. Hinton and E. Ruiz-Velasco. "Multi-messenger astronomy with very-high-energy gamma-ray observations". In: *Journal of Physics: Conference Series* 1468.1 (Feb. 2020), p. 012096. url: https://dx.doi.org/10.1088/1742-6596/1468/1/012096.

[14] S. Funk and J. Hinton. "Comparison of Fermi-LAT and CTA in the region between 10–100GeV". In: *Astroparticle Physics* 43 (2013). Seeing the High-Energy Universe with the Cherenkov Telescope Array - The Science Explored with the CTA, pp. 348–355. issn: 0927-6505. url: https://www.sciencedirect.com/science/article/pii/S0927650512001235.

[15] A. U. Abeysekara et al. “VERITAS Detection of LS 5039 and HESS J1825-137”. In: *Astroparticle Physics* 117, 102403 (Jan. 2020), p. 102403.

[16] H.E.S.S. Collaboration et al. “Particle transport within the pulsar wind nebula HESS J1825-137”. In: *A&A* 621 (2019), A116. URL: https://doi.org/10.1051/0004-6361/201834335.

[17] *TeVCat An Online Gamma-Ray Catalog.* http://tevcat.uchicago.edu/?mode=1&showsrc=115. Accessed: 2024-05-26.

[18] H. Uchiyama et al. “Suzaku Observation of HESS J1825-137: Discovery of Largely-Extended X-Rays from PSR J1826-1334”. In: *Publications of the ASJ* 61 (Jan. 2009), S189.

[19] B. M. Gaensler et al. “XMM-Newton Observations of PSR B1823-13: An Asymmetric Synchrotron Nebula around a Vela-like Pulsar”. In: *Astrophysical Journal* 588.1 (May 2003), pp. 441–451.

[20] G. G. Pavlov, O. Kargaltsev, and W. F. Brisken. “Chandra Observation of PSR B1823-13 and Its Pulsar Wind Nebula”. In: *Astrophysical Journal* 675.1 (Mar. 2008), pp. 683–694.

[21] F. Aharonian et al. “Energy dependent γ-ray morphology in the pulsar wind nebula HESS J1825-137”. In: *Astronomy and Astrophysics* 460.2 (Dec. 2006), pp. 365–374.

[22] H. E. S. S. Collaboration et al. “An extreme particle accelerator in the Galactic plane: HESS J1826-130”. In: *A&A* 644 (2020), A112. URL: https://doi.org/10.1051/0004-6361/202038851.

[23] C. L. Brogan et al. “Discovery of 35 New Supernova Remnants in the Inner Galaxy”. In: *Astrophysical Journal, Letters* 639.1 (Mar. 2006), pp. L25–L29.

[24] A. Albert et al. “Evidence of 200 TeV Photons from HAWC J1825-134”. In: *The Astrophysical Journal Letters* 907.2, L30 (Feb. 2021), p. L30.

[25] Planck Collaboration et al. “Planck 2015 results. X. Diffuse component separation: Foreground maps”. In: *Astronomy and Astrophysics* 594, A10 (Sept. 2016), A10.

[26] C. D. Rho, H. Ayala, and H. Zhou. “Techniques for Measuring Galactic Diffuse Emission Flux and their Preliminary Results in Confused Regions”. In: *ICRC* 35th International Cosmic Ray Conference — ICRC2017 (2017).

[27] A. U. Abeysekara et al. “Measurement of the Crab Nebula Spectrum Past 100 TeV with HAWC”. In: *Astrophysical Journal* 881.2, 134 (Aug. 2019), p. 134.

[28] F. Aharonian et al. “Observations of the Crab nebula with HESS”. In: *Astronomy and Astrophysics* 457.3 (Oct. 2006), pp. 899–915.

Eigenständigkeitserklärung

Hiermit versichere ich, Tobias Müller (Matrikelnummer: 22702504), die vorgelegte Arbeit selbstständig und ohne unzulässige Hilfe Dritter sowie ohne die Hinzuziehung nicht offengelegter und insbesondere nicht zugelassener Hilfsmittel angefertigt zu haben. Die Arbeit hat in gleicher oder ähnlicher Form noch keiner anderen Prüfungsbehörde vorgelegen und wurde auch von keiner anderen Prüfungsbehörde bereits als Teil einer Prüfung angenommen.

Die Stellen der Arbeit, die anderen Quellen im Wortlaut oder dem Sinn nach entnommen wurden, sind durch Angaben der Herkunft kenntlich gemacht. Dies gilt auch für Zeichnungen, Skizzen, bildliche Darstellungen sowie für Quellen aus dem Internet.

Mir ist insbesondere bewusst, dass die Nutzung künstlicher Intelligenz verboten ist, sofern diese nicht ausdrücklich als Hilfsmittel von dem Prüfungsleiter bzw. der Prüfungsleiterin zugelassen wurde. Dies gilt insbesondere für Chatbots (insbesondere ChatGPT) bzw. allgemein solche Programme, die anstelle meiner Person die Aufgabenstellung der Prüfung bzw. Teile derselben bearbeiten könnten.

Ort, Datum

Unterschrift